

## ORIGINAL ARTICLE

# Orientation Tuning and End-stopping in Macaque V1 Studied with Two-photon Calcium Imaging

Nian-Sheng Ju<sup>1</sup>, Shu-Chen Guan<sup>2</sup>, Louis Tao<sup>1</sup>, Shi-Ming Tang<sup>1,2,3</sup> and Cong Yu<sup>2,3,4</sup>

<sup>1</sup>School of Life Sciences, Peking University, Beijing 100181, China, <sup>2</sup>PKU-Tsinghua Center for Life Sciences, Peking University, Beijing 100181, China, <sup>3</sup>IDG-McGovern Institute for Brain Research, Peking University, Beijing 100181, China and <sup>4</sup>School of Psychology and Cognitive Sciences, Peking University, Beijing 100181, China

Address correspondence to Shi-Ming Tang, School of Life Sciences, Peking University, Beijing 100181, China. Email: tangshm@pku.edu.cn; Cong Yu, School of Psychology and Cognitive Sciences, Peking University, Beijing 100181, China. Email: yucong@pku.edu.cn.

Nian-Sheng Ju and Shu-Chen Guan are equal contribution co-first authors.

## Abstract

Orientation tuning is a fundamental response property of V1 neurons and has been extensively studied with single-/multiunit recording and intrinsic signal optical imaging. Long-term 2-photon calcium imaging allows simultaneous recording of hundreds of neurons at single neuron resolution over an extended time in awake macaques, which may help elucidate V1 orientation tuning properties in greater detail. We used this new technology to study the microstructures of orientation functional maps, as well as population tuning properties, in V1 superficial layers of 5 awake macaques. Cellular orientation maps displayed horizontal and vertical clustering of neurons according to orientation preferences, but not tuning bandwidths, as well as less frequent pinwheels than previous estimates. The orientation tuning bandwidths were narrower than previous layer-specific single-unit estimates, suggesting more precise orientation selectivity. Moreover, neurons tuned to cardinal and oblique orientations did not differ in quantities and bandwidths, likely indicating minimal V1 representation of the oblique effect. Our experimental design also permitted rough estimates of length tuning. The results revealed significantly more end-stopped cells at a more superficial 150 µm depth (vs. 300 µm), but unchanged orientation tuning bandwidth with different length tuning. These results will help construct more precise models of V1 orientation processing.

**Key words:** functional maps, macaque, orientation, primary visual cortex (V1), 2-photon calcium imaging

## Introduction

Since the discovery of V1 neurons' orientation selectivity (Hubel and Wiesel 1959, 1962), numerous studies have used single-/multiunit recording and intrinsic signal optical imaging (ISOI) to study V1 orientation tuning and functional organization. Yet many important issues (see below) are not fully understood, likely partly due to the technical limitations of these recording methods. For instance, single-/multiunit recording often under-samples neurons, and ISOI has very low signal-to-noise ratio and lacks cell-specific information.

In this study, we used long-term 2-photon calcium imaging to study orientation tuning of V1 superficial-layer neurons of

awake macaques. This technology allows simultaneous recording of hundreds of neurons' responses at single cell resolution over an extended time, overcoming some of the limitations of single-/multiunit recording and ISOI. We were particularly interested in two major issues. The first was the microstructures of functional maps of orientation tuning. Early single-unit recordings have revealed that V1 neurons are organized in columnar structures according to their preferred orientations (Hubel and Wiesel 1962, 1963). Later ISOI studies further suggest that different iso-orientation domains converge at singularity points to form pinwheels (Bonhoeffer and Grinvald 1991). However, Hubel and Wiesel (2005) disagreed on ISOI-based pinwheels because

these pinwheels are not centered on blobs where neurons have poor orientation tuning, likely an artifact caused by limited spatial resolution of ISOI (Polimeni et al. 2005). A full understanding of the functional organizations of V1 orientation tuning requires the knowledge of the microstructures of functional maps with cellular details. Our 2-photon imaging setup (Li et al. 2017) could image an  $850 \times 850\text{-}\mu\text{m}^2$  area, close to the size of a hypercolumn (Hubel and Wiesel 1977), which might be sufficient to reveal the microstructures of orientation maps.

The second major issue was the exact orientation tuning properties of V1 superficial-layer neurons. Superficial-layer neurons have narrower orientation tuning than those in middle and deeper layers (Schiller et al. 1976a; Ringach et al. 2002), so they are more likely involved in psychophysical orientation discrimination near threshold. Two-photon calcium imaging records large samples of neurons, including those with smaller cell bodies that are more likely missed by electrodes. Therefore, we expected to obtain more comprehensive and less biased results regarding distributions of orientation tuning bandwidths. With this information, computational models can more accurately use population coding to predict orientation discrimination thresholds (Vogels 1990).

In addition, because different stimulus sizes were used to approximate each neuron's maximal response in our study, the length tuning of each neuron and the percentages of neurons with end-stopping could be roughly estimated. Previous single-unit recordings indicated more end-stopped cells in superficial layers (Schiller et al. 1976b; Gilbert 1977). As our recordings were performed at 150-mm cortical depth, which was in layer 2, and at 300-mm cortical depth, which was likely on the layer 3 side of the layers 2 and 3 border (Ikezoe et al. 2013), we felt it tempting to find out whether the distributions of end-stopped cells at these 2 cortical depths could be different, which would reveal laminar-specific changes of end-stopping within superficial layers.

## Materials and Methods

### Monkey Preparation

Five macaque monkeys (Monkeys A–E, aged 5–8 years) participated in this study. In addition, data from a sixth monkey (Monkey F) in a separate ongoing study were also used to help analyze the time course of calcium signals (Fig. 1C bottom panel). Monkey preparations were identical to what reported in a previous paper (Guan et al. 2020). Each monkey was prepared with 2 sequential surgeries under general anesthesia and strictly sterile conditions. In the first surgery, a 20-mm diameter craniotomy was performed on the skull over V1. The dura was opened and multiple tracks of 100–150 nL AAV1.hSynap.GCaMP5G.WPRE.SV40 (AV-1-PV2478, titer 2.37e13 (GC/mL), Penn Vector Core) were pressure injected at a depth of  $\sim 350\text{ }\mu\text{m}$ . The dura was then sutured, then the skull cap was re-attached with 3 titanium lugs and 6 screws, and the scalp was sewn up. After the surgery, the animal was returned to the cage, treated with injectable antibiotics (Ceftriaxone sodium, Youcare Pharmaceutical Group, China) for 1 week. The second surgery was performed 45 days later. A T-shaped steel frame was installed for head stabilization, and an optical window was inserted onto the cortical surface. More details of the preparation and surgical procedures can be found in Li et al. (2017). The procedures were approved by the Institutional Animal Care and Use Committee, Peking University.

### Behavioral Task

After a 10-day recovery from the second surgery, monkeys were seated in a primate chair with head restraint. They were trained to hold fixation on a small white spot ( $0.1^\circ$ ) with eye positions monitored by an ISCAN ETL-200 infrared eye-tracking system (ISCAN Inc.) at a 120-Hz sampling rate. During the experiment, trials with the eye position deviated  $1.5^\circ$  or more from the fixation were discarded as ones with saccades and repeated. For the remaining trials, the eye positions were mostly concentrated around the fixation point. The mean and standard deviation of the eye positions from the fixation point were  $0.18^\circ$  and  $0.16^\circ$  for Monkey A,  $0.37^\circ$  and  $0.32^\circ$  for Monkey B,  $0.22^\circ$  and  $0.12^\circ$  for Monkey C,  $0.16^\circ$  and  $0.28^\circ$  for Monkey D, and  $0.23^\circ$  and  $0.20^\circ$  for Monkey E. The eye positions were within  $0.5^\circ$  from the fixation point in 96.5% of trials for Monkey A, 74.4% for Monkey B, 97.4% for Monkey C, 95.5% for Monkey D, and 92.9% for Monkey E.

### Visual Stimuli

Visual stimuli were generated by the ViSaGe system (Cambridge Research Systems) and presented on a 21" CRT monitor with a refresh rate of 80 Hz. Monitor resolution was set at 1280 pixel  $\times$  960 pixel. Because of the space and monitor screen size limits, viewing distances varied depending on the stimulus spatial frequency (30 cm at 0.25/0.5/1 cpd, 60 cm at 2 cpd, and 120 cm at 4/8 cpd).

A drifting square-wave grating (3 cycles/s, full contrast, 4 cpd spatial frequency, and  $0.4^\circ$  diameter in size) was first used to determine the population receptive field size and location associated with a recording site ( $2\text{--}4^\circ$  eccentricity), as well as ocular dominance columns when monocularly presented to confirm the V1 location. This process was quick with the use of a  $4\times$  objective lens mounted on the 2-photon microscope, which revealed no cell-specific information.

Cell-specific responses were then measured with a high-contrast (0.9) Gabor gating (Gaussian-windowed sinusoidal grating) drifting at 2 cycles/s in opposite directions perpendicular to the Gabor orientation. The Gabor grating varied at 12 equal-spaced orientations from  $0^\circ$  to  $165^\circ$  in  $15^\circ$  steps, and 6 spatial frequencies from 0.25 to 8 cpd in 1 octave steps. In addition, our pilot measurements suggested very strong surround suppression with larger stimuli. Therefore, we used 3 stimulus sizes at each spatial frequency, so as to estimate the best responses of each neuron with the most center summation and least surround suppression. Specifically, the  $\sigma$  of the Gaussian envelop of the Gabor were  $0.64\lambda$  and  $0.85\lambda$  at all SFs, and was additionally smaller at  $0.42\lambda$  when SFs were 0.25, 0.5, and 1 cpd, and larger at  $1.06\lambda$  when SFs were 2, 4, and 8 cpd ( $\lambda$ : wavelength; Gabors with the same  $\sigma$  in wavelength unit had the same number of cycles). Here at the smallest  $\sigma$  ( $0.42\lambda$ ), the Gabors still had sufficient number of cycles (frequency bandwidths = 1 octave) (Graham 1989), so that the actual stimulus SFs were precise at nominal values.

The stimuli at a specific viewing distance were pseudo-randomly presented. Each stimulus was presented for 1 s, with an interstimulus interval (ISI) of 1000 ms (Monkeys A and B) or 1500 ms (Monkeys C–E). As shown in Fig. 1C, at an ISI of 1000 ms, neural responses to optimal stimulus conditions were not fully back to the baseline level, which would affect F0 of the next trial, and thus the accuracy of orientation bandwidth estimation as discussed later. This issue

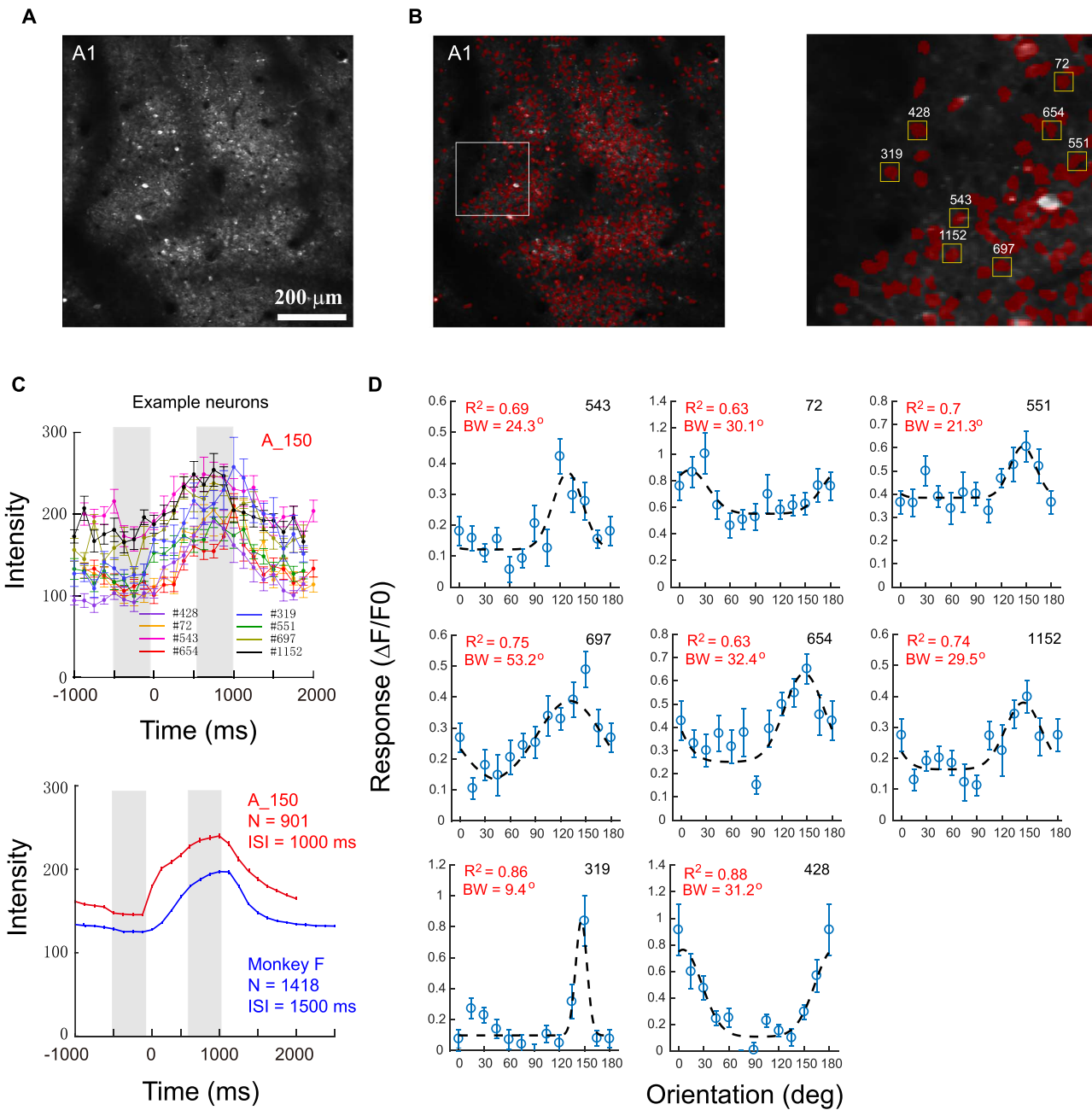


**Figure 1.** Two-photon calcium imaging and orientation tuning functions. (A) The average 2-photon image over a recording session at Monkey A recording site 1 at 150  $\mu\text{m}$  cortical depth (A1\_150). (B) Left: cell bodies extracted from A. Right: Zoomed-in view of the outlined area with 8 example neurons labeled. (C) The time course of calcium responses. Upper panel: the time courses of 8 example neurons at the preferred orientations and SFs. Lower panel: the red curve is the mean time course over all 901 orientation and SF tuned neurons at optimal orientation, SF, and size at A1\_150, with an ISI of 1000 ms. The blue curve is the mean time course over 1418 neurons, also at the optimal stimulus conditions, from Monkey F in a separate ongoing study with an ISI of 1500 ms. Each dot indicates one frame (8 f/s). After stimulus onset, the mean response started to saturate at around the 5th–6th frames (625–750 ms). The left shaded bars mark the 4 frames for calculating  $F_0$ , the baseline response. The right shaded bars mark the 4 frames for calculating  $F$ , the neuronal response. The interstimulus interval was 1000 ms for Monkeys A and B, and 1500 ms for Monkeys C–E. (D) Orientation responses of 8 example neurons and their Gaussian fittings. In some of these neurons, the responses at orientations orthogonal to the peak orientation were substantially higher than zero. These were likely real effects because the responses of the same neurons to nonoptimal spatial frequencies were near zero (to be presented in a separate paper). Neurons showing high-than-spontaneous activities at orthogonal orientations were also observed in a single-unit recording study (Ringach et al. 2002).  $R^2$  indicates the goodness-of-fit. BW indicates the orientation tuning bandwidth (half width at half height between the peak and minimal responses). Error bars represent  $\pm 1$  SEM.

was minimized when the ISI was extended to 1500 ms (see data from Monkey F in Fig. 1C lower panel). Each stimulus condition was repeated 10 times for Monkeys A and B, and 12 times for Monkeys C–E, with half trials for each opposite direction. Imaging of all orientations and spatial frequencies at a specific recording site and depth was completed in 1 session that lasted 3–4 h.

## Two-Photon Imaging

Two-photon imaging was performed with a Prairie Ultima IV (In Vivo) 2-photon microscope (Prairie Technologies) and a Ti:sapphire laser (Mai Tai eHP, Spectra Physics). One or two windows of  $850 \times 850 \mu\text{m}^2$  were selected in each animal and imaged using 1000-nm femtosecond laser under a 16× objective lens (0.8 N.A., Nikon) at a resolution of 1.6  $\mu\text{m}/\text{pixel}$ . Fast resonant scanning mode (32 fps) was chosen to obtain continuous images of neuronal activity (8 fps after averaging every 4 frames). Recordings at 2 depths for the same site were completed in 2 consecutive days. On the first day, recordings were performed at 150  $\mu\text{m}$ , and some neurons with high brightness or unique dendrite patterns were selected as landmarks. On the second day, the same field of view (FOV) at 150  $\mu\text{m}$  was first located with the help of landmark neurons. Then, the depth plane was lowered to 300  $\mu\text{m}$  for new recordings. This procedure was not strictly followed somehow for recordings at A2, so that the two FOVs were misaligned (Supplementary Fig. 1A).

## Imaging Data Analysis: Initial Screening of ROIs

Data were analyzed with customized MATLAB codes. A normalized cross-correlation-based translation algorithm was used to reduce motion artifacts (Li et al. 2017). Specifically, a template image was first generated by averaging 1000 successive frames in 1 imaging session. Two-photon images of 1 cortical area across days were then corrected and aligned using the template image. After the correction, fluorescence changes were associated with corresponding visual stimuli through the time sequence information recorded by Neural Signal Processor (Cerebus system, Blackrock Microsystem). By subtracting the mean of the 4 frames before stimuli onset ( $F_0$ ) from the average of the sixth–ninth frames after stimuli onset ( $F$ ) across 5 or 6 repeated trials for the same stimulus condition (same orientation, spatial frequency, size, and drifting direction), the differential image ( $\Delta F = F - F_0$ ) was obtained (Fig. 1A).

The regions of interest (ROIs) or possible neurons were decided through sequential analysis of 216 differential images in the order of SF (6), size (3), and orientation (12) ( $6 \times 3 \times 12 = 216$ ). The first differential image was filtered with a band-pass Gaussian filter (size = 2–10 pixels), and connected subsets of pixels (>25 pixels, which would exclude smaller vertical neuropils) with average pixel value >3 standard deviations of the mean brightness were selected as ROIs. Then, the areas of these ROIs were set to mean brightness in the next differential image before the bandpass filtering and thresholding were performed (This measure would eventually reduce the SDs of differential images and facilitate detection of neurons with relatively low fluorescence responses.) If a new ROI and an existing ROI from the previous differential image overlapped, the new ROI would be on its own if the overlapping area  $OA < 1/4 ROI_{new}$ , discarded if  $1/4 ROI_{new} < OA < 3/4 ROI_{new}$ , and merged with the existing ROI if  $OA > 3/4 ROI_{new}$ . The merges would help smooth the contours of

the final ROIs. This process went on through all 216 differential images twice to select ROIs. Finally, the roundness for each ROI was calculated as:

$$\text{Roundness} = \frac{\sqrt{4\pi \times A}}{P}$$

where  $A$  was the ROI's area and  $P$  was the perimeter. Only ROIs with roundness larger than 0.9, which would exclude horizontal neuropils, were selected as neurons for further analysis (Fig. 1B).

## Imaging Data Analysis: Orientation-Tuned Neurons

The ratio of fluorescence change ( $\Delta F/F_0$ ) was calculated as a neuron's response to a specific stimulus condition. For a specific cell's response to a specific stimulus condition, the  $F_{0n}$  of the  $n$ -th trial was the average of 4 frames before stimulus onset, and  $F_n$  was the average of fifth-eighth or sixth–ninth frames after stimulus onset, whichever was greater (Fig. 1C).  $F_{0n}$  was then averaged across 10 or 12 trials to obtain the baseline  $F_0$  for all trials (for the purpose of reducing noises in the calculations of responses), and  $\Delta F_n/F_0 = (F_n - F_0)/F_0$  was taken as the neuron's response to this stimulus at this trial. A small portion (~3%) of the neurons showed direction selectivity as their responses to 2 opposite directions differed significantly ( $P < 0.05$ , Friedman test). For those neurons, the 5–6 trials at the preferred direction were considered for calculations of  $\Delta F_n/F_0$  as the cell's responses to a particular stimulus.  $F_0$  was still averaged over 10–12 trials at 2 opposite directions.

Several steps were then taken to decide whether a neuron was tuned to orientation. First, the spatial frequency, orientation, and size producing the maximal response among all conditions were selected. Then responses to other 11 orientations were decided at the selected spatial frequency and size. Second, to select orientation tuned neurons, a non-parametric Friedman test was performed to test whether a neuron's responses at 12 orientations were significantly different from each other. To reduce type-I errors, the significance level was set at  $\alpha = 0.01$ . Third, for those showing significant difference, the orientation tuning function of each neuron was fitted with a Gaussian model:

$$R(\theta) = a_1 2^{-\left(\frac{\theta-\theta_0}{\sigma}\right)^2} + b$$

where  $R(\theta)$  was the response at orientation  $\theta$ , free parameters  $a_1$ ,  $\theta_0$ ,  $\sigma$ , and  $b$  were the amplitude, peak orientation, standard deviation of the Gaussian function, and minimal response of the neuron, respectively. Only neurons with the goodness of fit  $R^2 > 0.5$  were finally selected as orientation-tuned neurons (Fig. 1D). The amplitude parameter  $a_1$  was positive in all selected orientation neurons. In addition, we found that about 11% of neurons after Step 2 had 2 peaks in their orientation tuning functions as estimated in Monkey E, using a fitting model of Amirikian and Georgopoulos (2000), which matched the estimate (also 11% of V1 neurons) by David et al. (2006). These dual-peak neurons were not considered in further data analysis. Similar steps were also taken with a difference-of Gaussian model to decide whether a neuron is selective to spatial frequency, which will be detailed in a separate paper.

## Imaging Data Analysis: Pinwheels

To search pinwheels in an orientation map, the corresponding gradient map was calculated to show the local diversity of neuronal orientation preferences (Fig. 3). A discrete gradient map was first generated, in which each single neuron was pseudocolored by its gradient value. To calculate a target neuron's gradient value, neurons within 30 µm of the target were first selected. The difference of orientation preferences between each pair of the target neuron and one selected neuron was calculated, and then divided by the cortical distance of two neurons. The outcomes of all neuron pairs were averaged as the orientation gradient value of the target neuron. The gradient values of all neurons formed a discrete orientation gradient map, which was transformed to a continuous orientation gradient map with Gaussian filtering ( $\sigma = 15$  pixels). Then, the orientation gradient map was contour plotted (each contour contained dots having the same gradient values), and the same roundness equation used earlier for neuron selection was used to calculate the roundness of each contour:

$$\text{Roundness} = \frac{\sqrt{4\pi \times A}}{P}$$

This time A was the inner area of each contour and P was its perimeter. Since higher roundness indicated more pinwheel-like structures, a pinwheel was determined if 3 continuous concentric inner contours had  $R_s \geq 0.9$  in the orientation gradient map. In addition, to avoid artifacts caused by Gaussian smoothing, only those with the third inner contour containing 50 neurons were counted as pinwheels, with one exception (C1 in Fig. 3A), which contained 49 neurons.

## Results

We recorded orientation and SF responses in V1 superficial layers at 2–4° eccentricities in 5 awake macaques. Imaging processing and data analysis identified 17 280 ROIs or possible neurons. Among them, 14 791 were tuned to orientation and/or spatial frequency. Specifically, 12 468 (84.7%) were tuned to orientation, 10 205 (69.3%) to SF, and 7954 (54.0%) to both. The SF tuning results will be reported in a separate paper because of their volume and complexity.

### Orientation Functional Maps

Most neurons in orientation maps were clustered according to their preferred orientations (Fig. 2A). The distributions of orientation clusters appeared similar at 150 µm (Fig. 2A upper) and 300 µm (Fig. 2A lower) cortical depths, suggesting columnar structures. In maps A1, B, C1, and E where orientations were represented continuously in a full cycle (180°) or more, the orientation columns were arranged in parallel or crescent formations, and varied systematically. In A1 from the bottom up, and 30–40° right from vertical, the preferred orientation changed from orange/yellow-green (20°–60°) to orange/yellow-green (20°–60°) and then to purple (140°–160°), completing nearly 2 full cycles. In B, the preferred orientation changed from the bottom up in a crescent fashion, and in C1 and E from top-left to bottom-right in approximately a parallel fashion, to complete 1 full cycle. In A2 and D where some orientations were disproportionately represented, or in C2 where the orientation columns were less clear-cut, the preferred orientations also changed smoothly to neighboring ones.

To characterize the functional organizations of orientation tuning quantitatively, we calculated the differences of preferred orientations (DPOs) and tuning bandwidths (DBWs) between neuron pairs as a function of their absolute cortical distance. Fig. 2B shows the within-map pairwise DPOs, as well as simulated baselines with neuron positions shuffled (upper panel). The DPO functions intersected with the baselines at a cortical distance of mostly around 200–300 µm, which was the approximate width limit of orientation clusters. The strength of orientation clustering as a function of cortical distance was calculated as the inverse of the  $DPO_{\text{mean}}/DPO_{\text{baseline}}$  (lower panel), and the value within the first 50 µm of cortical distance was taken as the clustering index ( $CI > 1$  when neurons were clustered). Here, CI ranged from 2.53 to 5.19 (median = 3.57) over 7 recording sites, indicating horizontal neural clustering. Fig. 2C shows the functions of pairwise DPOs between 2 depths (upper panel) and the corresponding CIs (lower panel). Each pair included one neuron from 150 µm and the other from 300 µm depth. Again, the DPO functions intersected with the baselines at a cortical distance of about 200–300 µm. CI ranged from 2.52 to 3.93 (median = 3.34), indicating significant columnar structures (A2 excluded from analysis due to misaligned maps; Fig. 2C). The vertical clustering index was only 10% weaker than the horizontal clustering index ( $CI_V/CI_H = 89.5\%$ ;  $t_5 = 2.74$ ,  $P = 0.041$ , 2-tailed paired t-test; A2 excluded from analysis). However, horizontal clustering of orientation tuning bandwidth was nearly absent. The range of CI for bandwidth clustering (the inverse of  $DBW_{\text{mean}}/DBW_{\text{baseline}}$ ) was from 1.02 to 1.24, with a median of 1.13 (Fig. 3C).

### Pinwheels

To determine the pinwheels, orientation maps of two depths at the same site were summed (A2 excluded due to misalignment) to facilitate pinwheel detection (Ohki et al. 2006). Orientation gradient maps (Fig. 3A) were then calculated for all summed orientation maps, respectively (see Materials and Methods). A pinwheel was determined if its 3 inner contours' roundness values  $\geq 0.9$ , and the third most inner contour enclosed 50 or more neurons (C1 was an exception with 49 neurons). Only 1 pinwheel was detected in each map of A1, B, C1, and E, and none in C2, for a total of 5 pinwheels in 6 summed maps. This estimate of 0–1 pinwheels in a summed map was less than 2–3 pinwheels in similar-sized surface areas reported in previous ISOI (Lu and Roe 2008) and 2-photon imaging studies (Nauhaus et al. 2012, 2016) when maps were constructed with pixel-based orientation preferences. Furthermore, among the 5 pinwheels, only the 1 in Monkey D was detectable separately at each depth when only the roundness threshold was applied (Fig. 3B). The other 4 could not be detected separately at each depth because the roundness was less than the further lowered threshold  $R = 0.8$ . This difficulty of detecting pinwheels at a single depth was consistent with Ohki et al. (2006) that pinwheels may more likely reflect the organization of neurons summed over multiple depths.

There have been conflicting reports on whether orientation tuning bandwidths are wider in pinwheel neurons than in iso-domain neurons (Schummers et al. 2002; Nauhaus et al. 2008). We compared the orientation tuning bandwidths of neurons inside the third contour of the pinwheels in the orientation gradient maps (pinwheel neurons) and inside an annular area around the pinwheel center with the inner  $r = 180$  µm and outer  $r = 220$  µm (iso-domain neurons; those with the gradient  $> 0.5$

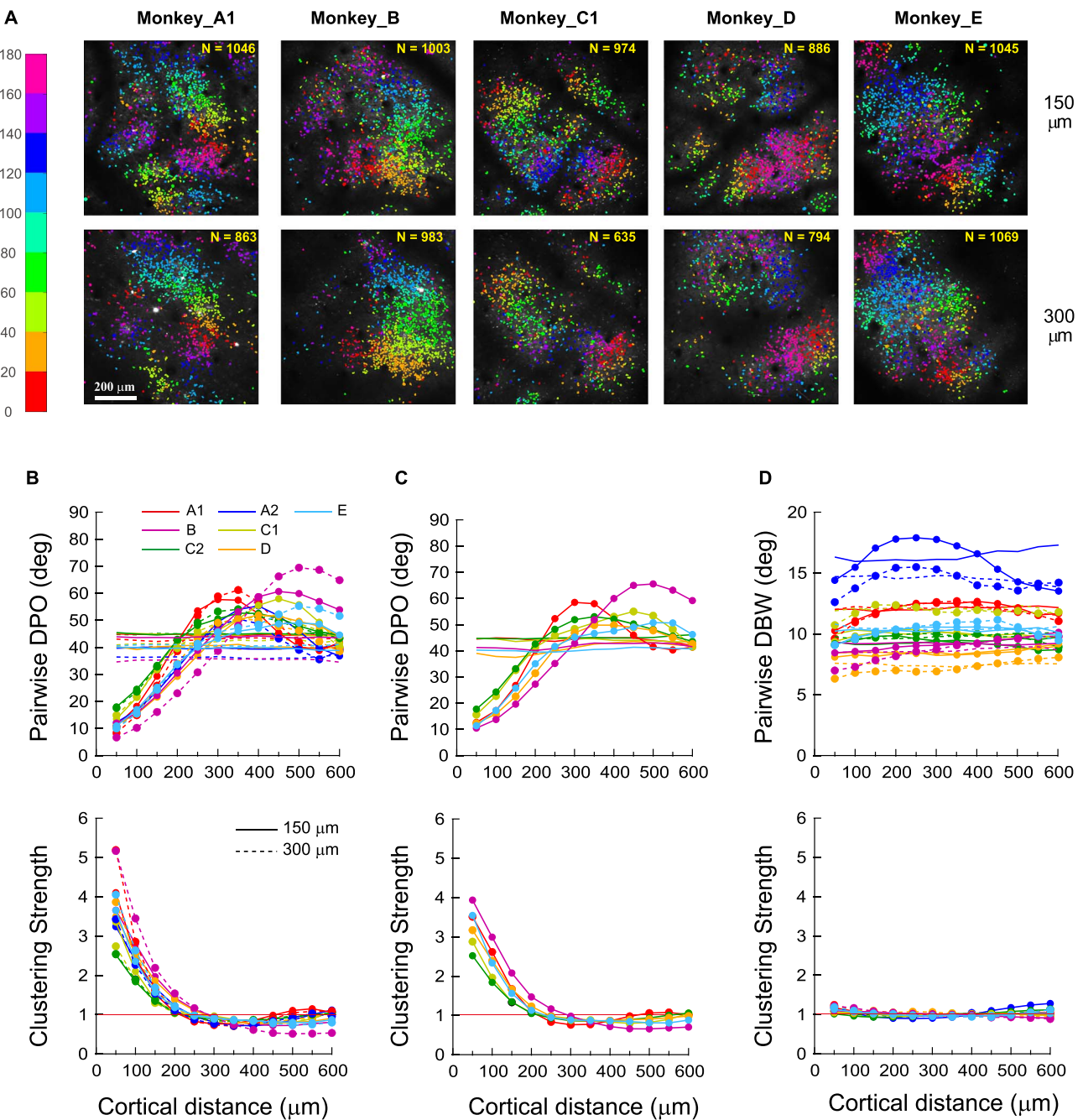


**Figure 2.** Orientation functional organizations. (A) Cellular orientation maps at 150 μm (upper) and 300 μm (lower) cortical depths. Recordings were performed at 2 sites in each of Monkeys A and B, and one site in each of Monkeys C–E (A2 and C2 orientation maps are represented in Supplementary Fig. 1). (B) Orientation clustering within the same maps. Upper: median within-map pairwise difference of preferred orientation (DPO) as a function of the absolute cortical distance. Each datum indicates the median pairwise DPO within a 50 μm bin up to the dot's corresponding cortical distance on the x-axis. Each corresponding horizontal line represents the baseline simulated with neurons shuffled in position. Lower: clustering strength. (C) Orientation columns across 2 depths. Upper: median across-depth pairwise DPO as a function of the absolute cortical distance. Every pair comprised one neuron from 150 μm and the other from 300 μm depth. Lower: clustering strength. (D) Orientation tuning bandwidth clustering within the same maps. Upper: median pairwise difference of orientation tuning bandwidth (DBW) as a function of the absolute cortical distance. Each datum indicates the median pairwise difference within a 50-μm bin up to the corresponding cortical distance on the x-axis. Each corresponding horizontal line represents the baseline simulated with the neurons shuffled in position. Lower: clustering strength. Error bars represent  $\pm 1$  SEM.

were excluded). The results showed no significant difference of bandwidths between 2 groups of neurons ( $t_4 = 1.145$ ,  $P = 0.32$ , 2-tailed paired t-test; Fig. 3C). The median bandwidth was wider with pinwheel neurons than with iso-domain neurons in Monkey D only, and was similar or narrower in other maps.

### Orientation Tuning Properties

The sharpness of neuronal orientation tuning is indicated by the tuning bandwidth. V1 superficial-layer neurons are known to have narrower tuning bandwidths than those in middle and deep layers (Schiller et al. 1976a; Ringach et al.

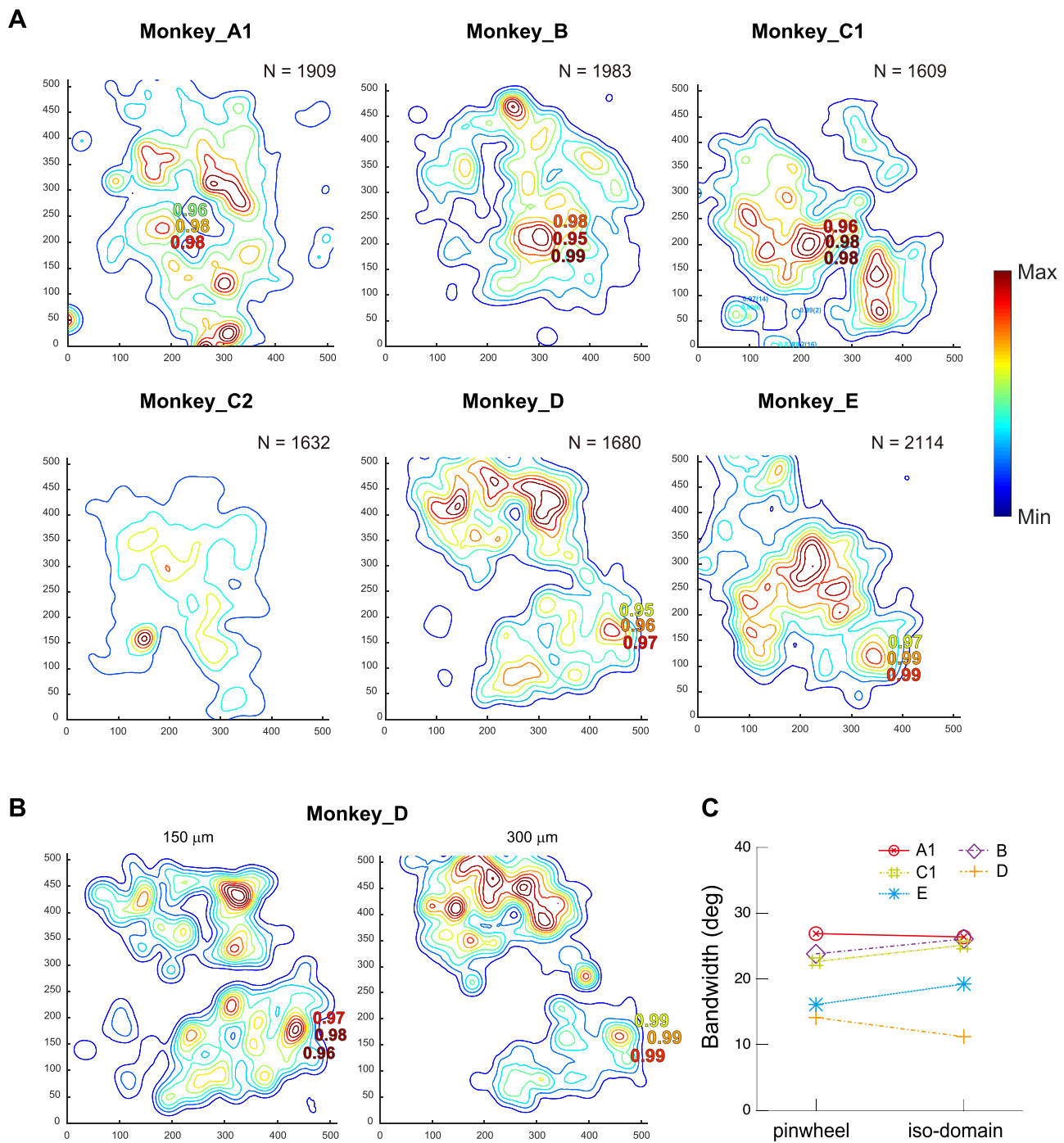


**Figure 3.** Pinwheels. (A) Orientation gradient maps for estimating pinwheels on the basis of summed maps over 2 recording depths (A2 excluded due to misalignment). Identified pinwheels are labeled with pinwheel metrics value for each contour. (B) The only pinwheel that could be detected at both cortical depths when only the roundness threshold was applied. (C) A comparison of median orientation bandwidths between pinwheel neurons and iso-domain neurons associated with 5 pinwheels.

2002), but the exact distributions of tuning bandwidth requires data from large samples of neurons. Fig. 4A shows that the medians of bandwidth (half width at half-height) distributions ranged from  $13.5^\circ$  to  $31.1^\circ$  (median =  $18.5^\circ$ , Fig. 4B). The median bandwidth was substantially narrower than the layer-specific estimate around  $28^\circ$  at comparable half-width at half-height (Ringach et al. 2002), but was closer to the estimate around

a median of  $22^\circ$  for parafoveal neurons by De Valois et al. (1982) (The originally reported bandwidth by Ringach et al. was approximately  $20^\circ$  at 70% height, which was equivalent to  $\sqrt{\log(0.5)/\log(0.7)} \times 20 = 28^\circ$  at half-height). However, we suspect that the shorter 1000-ms ISI in stimulus presentation might have partially contributed to the wider tuning bandwidths in Monkeys A and B, so that the actually bandwidth was closer to

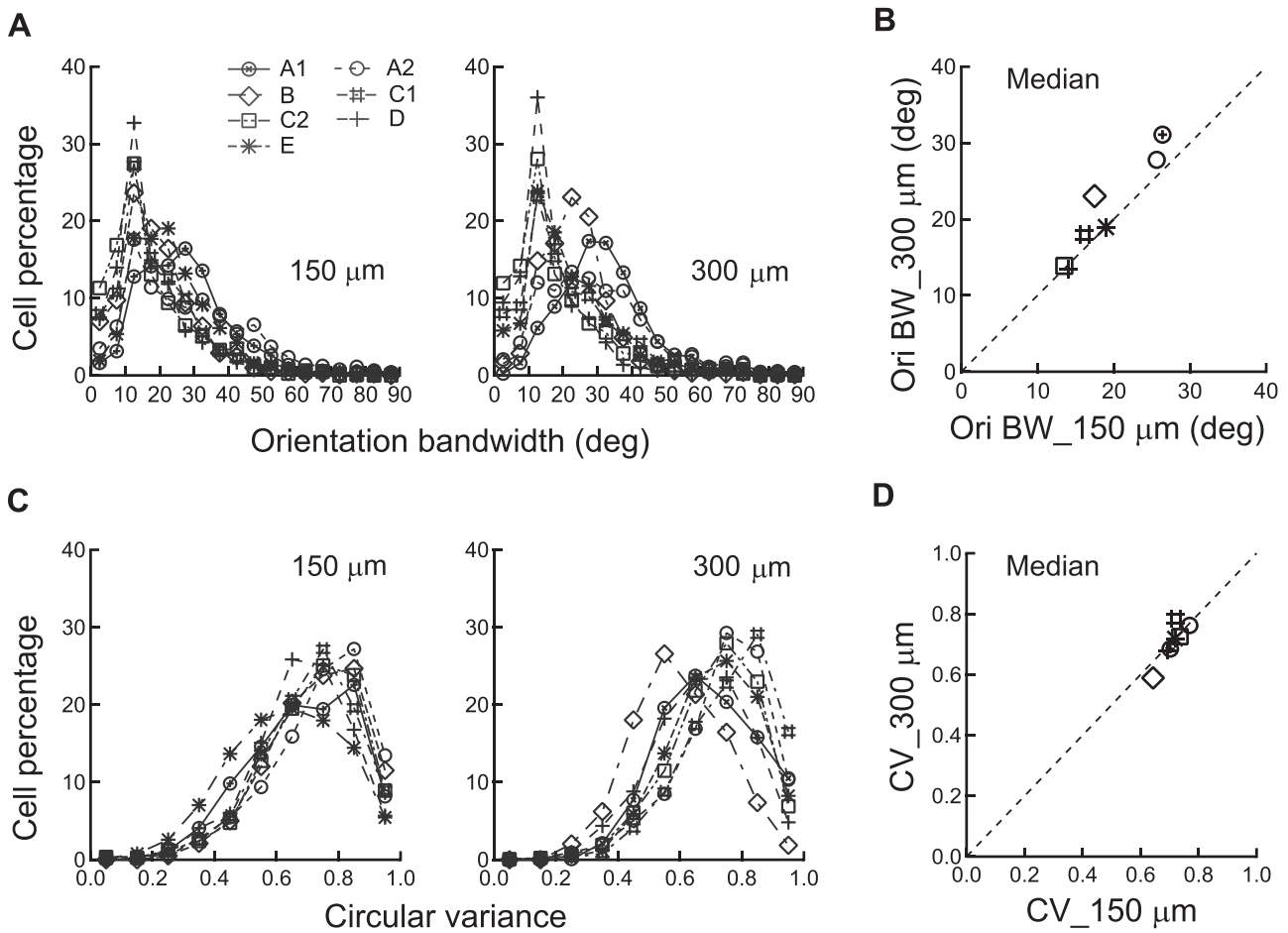


**Figure 4.** Orientation tuning properties in V1 superficial layers. (A) The percentage distributions of neurons as a function of orientation tuning bandwidth at 150 and 300  $\mu\text{m}$ , respectively. (B) Median orientation tuning bandwidths at 300 vs. 150  $\mu\text{m}$  for each recording site. (C) The percentage distributions of neurons as a function of circular variance at 150 and 300  $\mu\text{m}$ , respectively. (D) Median circular variances at 300 vs. 150  $\mu\text{m}$  for each recording site.

the estimates from the other 3 monkeys with an ISI of 1500 ms (e.g., median = 15.1°), which will be discussed later. The grand median bandwidth of all neurons at 150  $\mu\text{m}$  was 19.0°, narrower than 20.9° at 300  $\mu\text{m}$ . This difference was mainly contributed by A1 and B (Fig. 4B), and thus might not be a general effect.

In an earlier 2-photon imaging study using anesthetized monkeys, Ikezoe et al. (2013) reported that the median circular variance of V1 neurons, which is a global index of the shape of orientation tuning functions in contrast to local orientation selectivity measured by orientation bandwidth (Ringach et al. 2002), was 0.78 when all neurons were considered. We found a similar median circular variance (0.72) that did not differ significantly at 150 and 300  $\mu\text{m}$  cortical depths ( $t_6 = 0.68, P = 0.52$ , 2-tailed paired t-test) (Fig. 4C,D). These CV ranges were larger (or weaker orientation tuning) than those (median < 0.5) from single-unit recordings of superficial layer neurons in macaques (Ringach et al. 2002). Therefore, 2-photon calcium imaging appeared to reveal narrower orientation tuning bandwidths, but larger circular variances, than single-unit recordings.

### Orientation Anisotropies

Humans are more sensitive to cardinal (horizontal/vertical) than to oblique orientations (Campbell and Kulikowski 1966).

Whether and how this oblique effect is represented in V1 has been a topic of debate (Hubel and Wiesel 1968; De Valois et al. 1982; Li et al. 2003; Freeman et al. 2011; Alink et al. 2013; Shen et al. 2014). A repeated-measures ANOVA indicated that the percentages of neurons preferring different orientations, including the cardinal and oblique orientations, were similar across orientations ( $F_{1,66} = 0.61, P = 0.812$ ) and between depths ( $F_{1,6} = 0.00, P = 1.000$ ) (Fig. 5A). So were the orientation tuning bandwidths across orientations ( $F_{1,66} = 0.73, P = 0.704$ ) and between depths ( $F_{1,6} = 2.32, P = 0.178$ ) (Fig. 5B). Therefore, our results do not support V1 representations of the oblique effect.

Humans are also more sensitive to radial than to tangential orientations relative to the fovea (Westheimer 2003). Our results showed that, on average, more neurons preferred the radial orientation to tangential orientation at 300  $\mu\text{m}$ , but not at 150  $\mu\text{m}$  (Fig. 5C). A repeated-measures ANOVA that indicated a significant main effect of orientation ( $F_{1,66} = 2.42, P = 0.013$ ) and a significant interaction between orientation and depth ( $F_{1,66} = 4.11, P < 0.001$ ) (Fig. 5C), while the main effect of depth was insignificant ( $F_{1,6} = 0.00, P = 1.000$ ). A contrast analysis showed a significant difference between the radial and tangential orientations (indicated by R and T in x-axes, each including a ±7.5° orientation range,  $t_{66} = 2.90, P = 0.007$ ), suggesting a

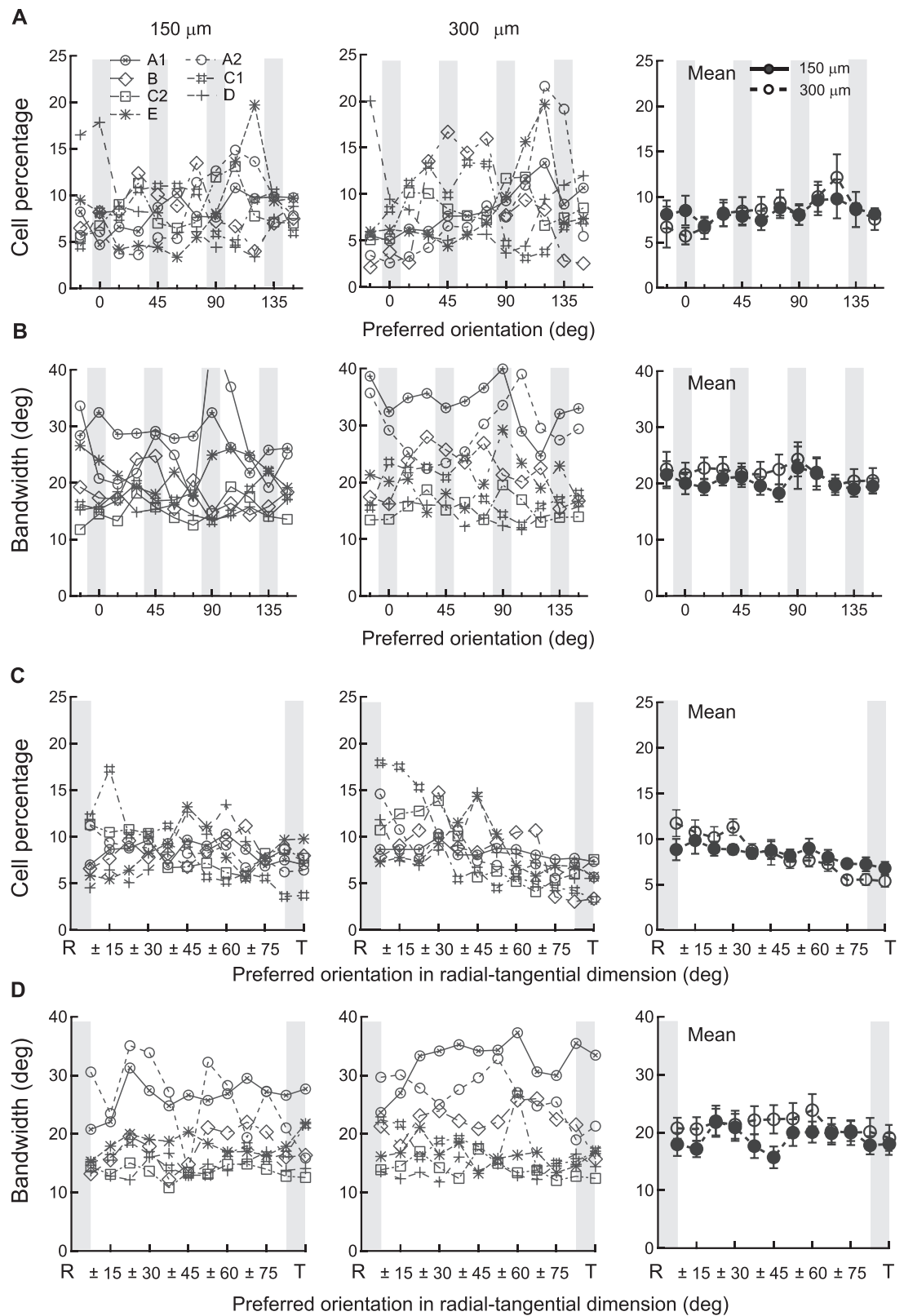


**Figure 5.** Oblique effect and radial-tangential anisotropy. (A,B) Oblique effects. Distributions of percentage (A) and tuning bandwidth (B) against preferred orientations. (C, D) Radial-tangential anisotropy. Distributions of percentage (C) and tuning bandwidth (D) against preferred orientations along the radial-tangential continuum. In all subfigures, each datum in the left 2 panels (150 and 300  $\mu\text{m}$ ) indicates the median of a bin ranging  $\pm 7.5^\circ$  of the preferred orientation on the x-axis. The means are the averages of medians of individual maps. Error bars represent  $\pm 1$  SEM.

radial-tangential anisotropy. Meanwhile, there were no significant main effects of orientation ( $F_{11,66} = 1.32$ ,  $P = 0.232$ ) and depth ( $F_{1,6} = 2.25$ ,  $P = 0.184$ ) for orientation tuning bandwidths (Fig. 5D). The radial-tangential difference of percentage distributions of neurons may be taken with caution, as large variations existed among the maps. For example, maps of D and E at both depths displayed substantially higher percentages of neurons around  $30^\circ$ – $70^\circ$  along the radial-tangential continuum.

### End-stopping

Among all orientation-tuned neurons, 57.0% exhibited significant differences of responses at 3 stimulus sizes (Friedman test) at the optimal orientations. We categorized those showing maximal responses at small and intermediate sizes as end-stopped neurons, and those at the large size as end-free neurons. This was a rough approximation since the “end-free” neurons were likely mixed with end-stopped neurons tuned to the large stimulus size or even larger sizes. Responses of 22.3% neurons maximized at the small size at  $150\text{ }\mu\text{m}$ , higher than 15.5% neurons at deeper  $300\text{ }\mu\text{m}$ , while similar percentages of neurons (15.8% at  $150\text{ }\mu\text{m}$  and 13.9% at  $300\text{ }\mu\text{m}$ ) maximized at the intermediate size (Fig. 6A). A repeated-measures ANOVA indicated a significant main effect of stimulus size ( $F_{1,6} = 18.16$ ,  $P = 0.005$ ), and a significant interaction between stimulus size and depth ( $F_{1,6} = 7.38$ ,  $P = 0.035$ ). Together, 38.8% neurons were end-stopped at  $150\text{ }\mu\text{m}$ , in comparison with 29.5% at  $300\text{ }\mu\text{m}$ . However, regardless of being end-stopped or not, there was no significant main effects of stimulus size ( $F_{2,12} = 2.21$ ,  $P = 0.153$ ) and cortical depth ( $F_{1,6} = 1.66$ ,  $P = 0.245$ ) for orientation tuning bandwidth (Fig. 6B).

Some early reports indicated that in cat area 17 the oblique effect was limited to 1 type (S type) of end-free simple cells (Orban and Kennedy 1981; Orban et al. 1984). The slow calcium responses made it impossible to track the phase effects of a drifting grating, so we were not able to separate simple and complex cells. Here, we only compared the oblique effects with end-stopped and end-free cells (Fig. 6C). For each recording site, neurons were pooled over 2 recording depths. A mixed-design ANOVA indicated no significant differences of the percentages of neurons preferring different orientations, including the cardinal and oblique orientations, ( $F_{11,132} = 0.997$ ,  $P = 0.453$ ), and between end-stopped and end-free cells ( $F_{1,12} = 0.00$ ,  $P = 0.997$ ).

### Discussion

In this study, we investigated orientation tuning in superficial-layer neurons of macaque V1. The orientation maps confirmed horizontal and vertical clustering of orientation preferences, but revealed no clustering of tuning bandwidths and less frequent pinwheels. The orientation tuning bandwidths were narrower than previous estimates, and there was no evidence for a significant V1 representation of the oblique effect. In addition, there appeared to be more end-stopped neurons, especially those tuned to shorter lengths, at more superficial cortical depth within the superficial layers.

Previously, we have shown that monkey 2-photon calcium imaging produces consistent data, in that neurons' preferred orientations measured with drifting gratings were still highly correlated ( $r = 0.87$ ) when the test and retest were separated by 4 months (Ju et al. 2018). Here, the confirmation of iso-orientation clusters suggests that 2-photon calcium imaging is a reliable tool to study neural functions in the visual cortex

of awake monkeys, which would help validate future findings using the same method. Moreover, some discrepancies in the distribution of orientation tuning bandwidth and the oblique effect, which are known to be susceptible to neural undersampling and sampling biases, may be demonstrations of the powerfulness of this new technology.

Our cellular orientation maps pooled over 2 cortical depths revealed 0–1 pinwheels in an area of approximately 1 hypercolumn. A previous 2-photon imaging study on anesthetized monkeys, which had small imaging areas (maximal  $279 \times 279\text{ }\mu\text{m}$  about one-ninth of ours, revealed no pinwheels (Ikezoe et al. 2013). In contrast, about 2–3 pinwheels have been shown in areas of pixel-based orientation maps similar to ours, obtained with either ISOI or 2-photon imaging (Lu and Roe 2008; Nauhaus et al. 2012; Nauhaus et al. 2016). The exact pinwheel frequency may be difficult to decide due to technical limitations of all methods. In our study, viral expression would label less neurons than OGB injection as in Nauhaus et al. (2012) and Nauhaus et al. (2016). Although the summed maps contained 1600–2100 neurons in each  $850 \times 850\text{-}\mu\text{m}^2$  area, more complete labeling of neurons, or more neurons summed from more than 2 depths, could potentially reveal more pinwheels. In addition, blood vessels might have also masked potential pinwheels. On the other hand, the frequencies of pinwheels observed in ISOI studies (Bonhoeffer and Grinvald 1991; Lu and Roe 2008) are affected by image processing that could produce false pinwheels (Polimeni et al. 2005). In addition, in Nauhaus et al. (2012) and Nauhaus et al. (2016), the frequencies of pinwheels in similar-sized areas ( $800 \times 800\text{ }\mu\text{m}^2$ ) are only available in pixel-based maps (cellular details are available in  $200 \times 200\text{ }\mu\text{m}^2$  areas only), which could also be affected by image processing.

Previous evidence has shown that V1 superficial-layer neurons have narrower orientation tuning than those in middle and deep layers, with a median bandwidth of about  $20^\circ$  at half-width and 70% height (Ringach et al. 2002), which would be approximately  $28^\circ$  at 50% height (also see Schiller et al. 1976b). Narrower bandwidths of parafoveal neurons ( $22$ – $23^\circ$  at half width and half height) were also reported by De Valois et al. (1982) and David et al. (2006). Our 2-photon results revealed overall narrower tuning bandwidths (median =  $18.5^\circ$ ) at half width and half height. Moreover, wider tuning bandwidths in Monkeys A and B ( $17.5$ – $31.1^\circ$ , median =  $26.0^\circ$ ) might be at least partially related to the shorter 1000-ms ISI as the bandwidths in other 3 monkeys, which were tested with 1500-ms ISI, were narrower ( $13.5$ – $21.7^\circ$ , median =  $15.1^\circ$ ). As shown in Fig. 1C, an ISI of 1000 ms increased the chance that a new trial started before complete decay of the calcium signal from the previous trial, which would make responses to different orientations more similar and increase the bandwidth artificially. This problem was minimized when the calcium signals were fully back to the baseline level with an ISI of 1500 ms. Therefore, overall the actual orientation bandwidth could be more like those estimated with 1500 ms ISIs and substantially narrower than previous results. It is likely that more narrowly tuned neurons had been under-sampled by electrodes in previous studies. Nevertheless, our new estimates suggest that V1 orientation processing is likely more precise than previously assumed. Therefore, a smaller number of neurons are required to produce fine orientation thresholds through population coding (Vogels 1990).

Single-unit evidence for V1 representation of the oblique effect has been mixed. Hubel and Wiesel (1968) failed to observe the oblique effect in V1 neuron distributions, and De Valois et al. (1982) only found the effect in foveal neurons within  $1^\circ$

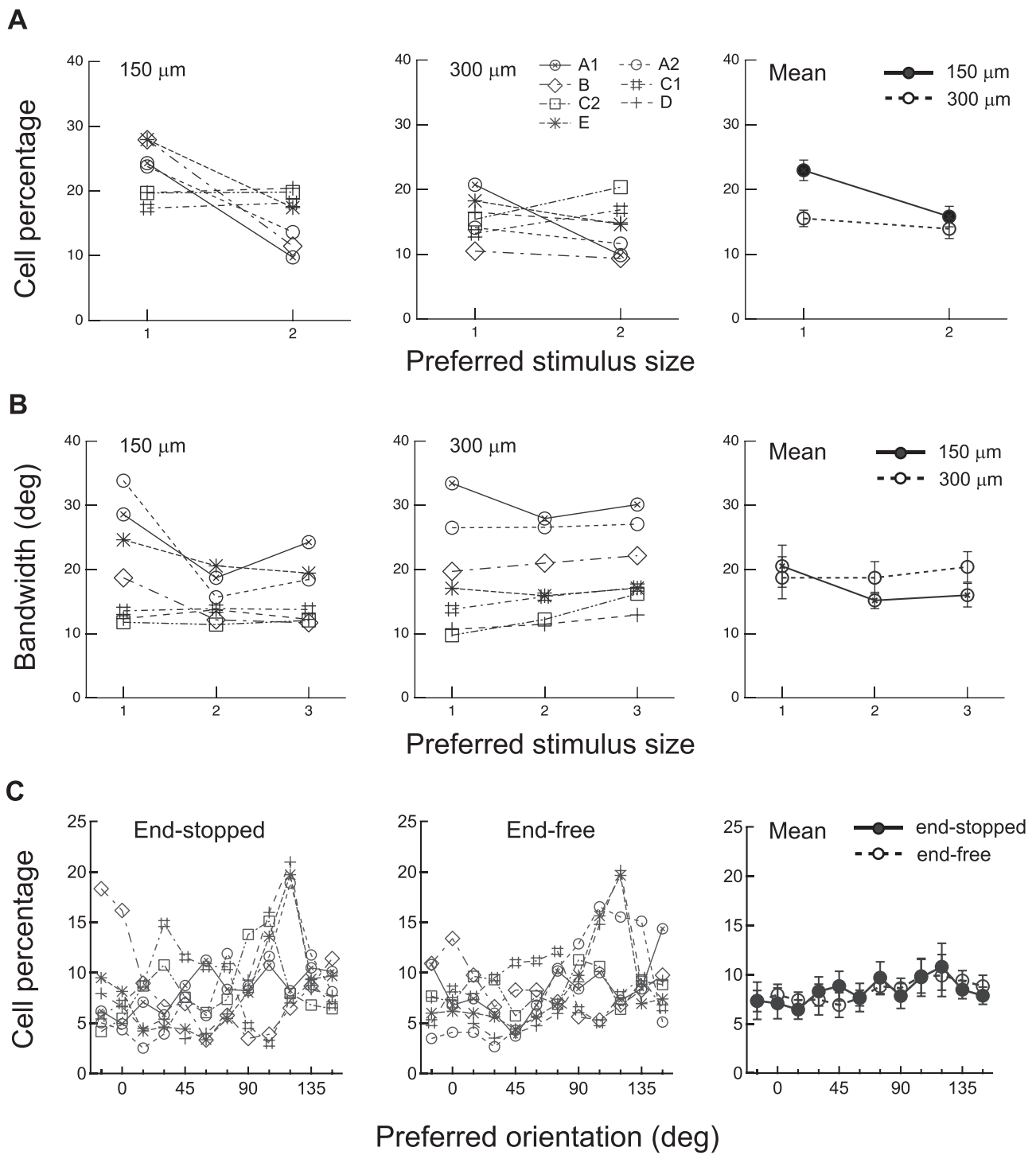


**Figure 6.** End-stopping in V1 superficial-layer neurons. (A) Percentages of neurons that are end-stopped at 150  $\mu\text{m}$  (solid lines) and 300  $\mu\text{m}$  (dashed lines). (B) Orientation tuning bandwidths as a function of length tuning at 2 cortical depths. (C) A comparison of the oblique effect in end-stopped and end-free neurons. Each datum in the left 2 panels (end-stopped and end-free) indicates the median of a bin ranging  $\pm 7.5^\circ$  of the preferred orientation on the x-axis. The means in the right panel are the averages of medians of individual maps for end-stopped and end-free cells, respectively. Error bars represent  $\pm 1$  SEM.

eccentricity, even if the oblique effect can be measured psychophysically in peripheral locations up to  $10^\circ$  eccentricity (Vandenbussche et al. 1986). A meta-analysis reveals that more simple cells are tuned to the horizontal orientation with narrower tuning bandwidths in the cat striate cortex, but the analysis

fails to suggest an over-representation of the vertical orientation (Li et al. 2003). Considering that superficial-layer neurons have the best orientation tuning (Schiller et al. 1976a; Ringach et al. 2002) and are thus mostly likely responsible for fine orientation discrimination, our results, showing no difference of neuron

quantities and bandwidths among preferred orientations, do not support V1 representations of the oblique effect. Because the oblique effect is observable with orientations defined by non-V1 stimuli like a pair of dots, it could occur beyond V1 (Westheimer 2003). This possibility is echoed by a more recent single-unit report that the oblique effect is represented in macaque V2, but not V1 (Shen et al. 2014). Moreover, orientation bias could be shaped by experience with non-uniform natural image statistics, as demonstrated through training of a convolutional neural network (Henderson and Serences 2020). As a result, the oblique effect does not necessarily require biases in the distribution of neuronal orientation preference or tuning bandwidth. Rather, biased feature attention and decision-making that match the natural image statistics could also lead to differences in orientation thresholds between cardinal and oblique orientations.

End-stopped cells are more prevalent in V1 superficial-layers (Schiller et al. 1976b; Gilbert 1977). Our results showed that within the superficial-layers, more end-stopped cells, which were mainly those tuned to the short stimuli, were present at a more superficial depth (150 vs. 300 µm) (Fig. 6). It is likely that end-stopping as an emergent response property of V1 becomes finer-tuned to stimulus length as neurons become more downstream within the superficial layers. Nevertheless, the current estimates are very coarse as only 3 stimulus sizes were used. We plan to perform more detailed recordings of length tuning, as well as curvature responses, in a new study.

## Supplementary Material

Supplementary material can be found at *Cerebral Cortex* online.

## Notes

We thank Geoff Ghose, Stanley Klein, Haidong Lu, Guy Orban, and Rufin Vogels for their very helpful comments and suggestions. Conflict of Interest: None declared.

## Funding

Natural Science Foundation of China (grants 31230030 and 31730179); Peking-Tsinghua Center for Life Sciences, Peking University.

## References

- Alink A, Krugliak A, Walther A, Kriegeskorte N. 2013. fMRI orientation decoding in V1 does not require global maps or globally coherent orientation stimuli. *Front Psychol.* 4:493.
- Amirikian B, Georgopoulos AP. 2000. Directional tuning profiles of motor cortical cells. *Neurosci Res.* 36:73–79.
- Bonhoeffer T, Grinvald A. 1991. Iso-orientation domains in cat visual cortex are arranged in pinwheel-like patterns. *Nature.* 353:429–431.
- Campbell FW, Kulikowski JJ. 1966. Orientational selectivity of the human visual system. *J Physiol.* 187:437–445.
- David SV, Hayden BY, Gallant JL. 2006. Spectral receptive field properties explain shape selectivity in area V4. *J Neurophysiol.* 96:3492–3505.
- De Valois RL, Yund EW, Hepler N. 1982. The orientation and direction selectivity of cells in macaque visual cortex. *Vision Res.* 22:531–544.
- Freeman J, Brouwer GJ, Heeger DJ, Merriam EP. 2011. Orientation decoding depends on maps, not columns. *J Neurosci.* 31:4792–4804.
- Gilbert CD. 1977. Laminar differences in receptive field properties of cells in cat primary visual cortex. *J Physiol.* 268:391–421.
- Graham N. 1989. *Visual pattern analyzers*. Oxford psychology series, Vol. 16. Oxford University Press, New York.
- Guan SC, Zhang SH, Zhang YC, Tang S, Yu C. 2020. Plaid detectors in macaque V1 revealed by two-photon calcium imaging. *Curr Biol.* 30:934–940.
- Henderson M, Serences J. 2020. Biased orientation representations can be explained by experience with non-uniform training set statistics. *bioRxiv*. doi: [10.1101/2020.11.17.209536](https://doi.org/10.1101/2020.11.17.209536).
- Hubel DH, Wiesel TN. 1959. Receptive fields of single neurones in the cat's striate cortex. *J Physiol.* 148:574–591.
- Hubel DH, Wiesel TN. 1962. Receptive fields, binocular interaction and functional architecture in the cat's visual cortex. *J Physiol.* 160:106–154.
- Hubel DH, Wiesel TN. 1963. Shape and arrangement of columns in cat's striate cortex. *J Physiol.* 165:559–568.
- Hubel DH, Wiesel TN. 1968. Receptive fields and functional architecture of monkey striate cortex. *J Physiol.* 195:215–243.
- Hubel DH, Wiesel TN. 1977. Ferrier lecture. Functional architecture of macaque monkey visual cortex. *Proc R Soc Lond B Biol Sci.* 198:1–59.
- Hubel DH, Wiesel TN. 2005. *Brain and visual perception*. New York: Oxford Press.
- Ikezoe K, Mori Y, Kitamura K, Tamura H, Fujita I. 2013. Relationship between the local structure of orientation map and the strength of orientation tuning of neurons in monkey V1: a 2-photon calcium imaging study. *J Neurosci.* 33:16818–16827.
- Ju N, Jiang R, Macknik SL, Martinez-Conde S, Tang S. 2018. Long-term all-optical interrogation of cortical neurons in awake-behaving nonhuman primates. *PLoS Biol.* 16:e2005839.
- Li B, Peterson MR, Freeman RD. 2003. Oblique effect: a neural basis in the visual cortex. *J Neurophysiol.* 90:204–217.
- Li M, Liu F, Jiang H, Lee TS, Tang S. 2017. Long-term two-photon imaging in awake macaque monkey. *Neuron.* 93:1049, e1043–1057.
- Lu HD, Roe AW. 2008. Functional organization of color domains in V1 and V2 of macaque monkey revealed by optical imaging. *Cereb Cortex.* 18:516–533.
- Nauhaus I, Benucci A, Carandini M, Ringach DL. 2008. Neuronal selectivity and local map structure in visual cortex. *Neuron.* 57:673–679.
- Nauhaus I, Nielsen KJ, Callaway EM. 2016. Efficient receptive field tiling in primate V1. *Neuron.* 91:893–904.
- Nauhaus I, Nielsen KJ, Disney AA, Callaway EM. 2012. Orthogonal micro-organization of orientation and spatial frequency in primate primary visual cortex. *Nat Neurosci.* 15:1683–1690.
- Ohki K, Chung S, Kara P, Hubener M, Bonhoeffer T, Reid RC. 2006. Highly ordered arrangement of single neurons in orientation pinwheels. *Nature.* 442:925–928.
- Orban GA, Kennedy H. 1981. The influence of eccentricity on receptive field types and orientation selectivity in areas 17 and 18 of the cat. *Brain Res.* 208:203–208.
- Orban GA, Vandebussche E, Vogels R. 1984. Human orientation discrimination tested with long stimuli. *Vision Res.* 24:121–128.
- Polimeni JR, Granquist-Fraser D, Wood RJ, Schwartz EL. 2005. Physical limits to spatial resolution of optical recording:

- clarifying the spatial structure of cortical hypercolumns. *Proc Natl Acad Sci USA*. 102:4158–4163.
- Ringach DL, Shapley RM, Hawken MJ. 2002. Orientation selectivity in macaque V1: diversity and laminar dependence. *J Neurosci*. 22:5639–5651.
- Schiller PH, Finlay BL, Volman SF. 1976a. Quantitative studies of single-cell properties in monkey striate cortex. I. Spatiotemporal organization of receptive fields. *J Neurophysiol*. 39:1288–1319.
- Schiller PH, Finlay BL, Volman SF. 1976b. Quantitative studies of single-cell properties in monkey striate cortex. II. Orientation specificity and ocular dominance. *J Neurophysiol*. 39:1320–1333.
- Schummers J, Marino J, Sur M. 2002. Synaptic integration by V1 neurons depends on location within the orientation map. *Neuron*. 36:969–978.
- Shen G, Tao X, Zhang B, Smith EL 3rd, Chino YM. 2014. Oblique effect in visual area 2 of macaque monkeys. *J Vis*. 14(2):3, 1–16.
- Vandenbussche E, Vogels R, Orban GA. 1986. Human orientation discrimination: changes with eccentricity in normal and amblyopic vision. *Invest Ophthalmol Vis Sci*. 27:237–245.
- Vogels R. 1990. Population coding of stimulus orientation by striate cortical cells. *Biol Cybern*. 64:25–31.
- Westheimer G. 2003. The distribution of preferred orientations in the peripheral visual field. *Vision Res*. 43:53–57.